Direct Observation of Martensitic Phase-Transformation Dynamics in Iron by 4D Single-Pulse Electron Microscopy

Hyun Soon Park, Oh-Hoon Kwon, J. Spencer Baskin, Brett Barwick, and Ahmed H. Zewail*

Physical Biology Center for Ultrafast Science and Technology, Arthur Amos Noyes Laboratory of Chemical Physics, California Institute of Technology, Pasadena, California 91125

ABSTRACT

The in situ martensitic phase transformation of iron, a complex solid-state transition involving collective atomic displacement and interface movement, is studied in real time by means of four-dimensional (4D) electron microscopy. The iron nanofilm specimen is heated at a maximum rate of $\sim 10^{11}$ K/s by a single heating pulse, and the evolution of the phase transformation from body-centered cubic to face-centered cubic crystal structure is followed by means of single-pulse, selected-area diffraction and real-space imaging. Two distinct components are revealed in the evolution of the crystal structure. The first, on the nanosecond time scale, is a direct martensitic transformation, which proceeds in regions heated into the temperature range of stability of the fcc phase, 1185−1667 K. The second, on the microsecond time scale, represents an indirect process for the hottest central zone of laser heating, where the temperature is initially above 1667 K and cooling is the rate-determining step. The mechanism of the direct transformation involves two steps, that of (barrier-crossing) nucleation on the reported nanosecond time scale, followed by a rapid grain growth typically in ~ 100 ps for 10 nm crystallites.

Iron (Fe) is a material of vital importance to the Earth sciences and condensed matter physics, and it remains the defining metal for many technological applications.[1] The fundamental, physical properties at high temperatures and/ or high pressures have been intensively investigated, leading to rich information for its allotropic transformation and the associated phase diagram.[2,3] Iron occurs in three distinct polymorphs: the body-centered cubic (bcc) and the face-centered cubic (fcc) at one atmosphere, and the hexagonal close packed (hcp) at high pressures. While the physical properties of the hcp phase at high pressures (and high temperatures) are of greatest importance to geophysicists investigating the nature of Earth's core,[4,5] the unique Fe transformation between the high-temperature fcc and low-temperature bcc structures lies at the core of steel technology and crystallography for producing a wide variety of micro-structures with corresponding variations in physical charac-teristics.[6,7] The present picture is that Fe exists under ambient conditions in the ferromagnetic, bcc phase (α-Fe), and above the Currie temperature of 1043 K the α-Fe changes into paramagnetic β-Fe of the same structure, that is, bcc.[8] The fcc structure (γ-Fe) is stable at temperatures above 1185 K. The recurrence of the bcc structure (δ-Fe) is observed between 1667 K and the melting point at 1811 K.[8]

The phase transition between these bcc and fcc structures in Fe is a typical example of martensitic transformation, so-called diffusionless or displacive transformation, which is a classic topic studied extensively over the past century and remains an important subject of research in materials science.[6−11] The thermodynamic and crystallographic proper-ties involved have been examined using a variety of techniques such as optical microscopy, X-ray diffraction, and electron microscopy.[6−12] In contrast to diffusion-controlled phase transitions, the martensitic transformation is a collec-tive phenomenon where a crystal undergoes a first-order change from one structure to another involving synchronous movements of many atoms with atomic amplitudes less than the dimension of the lattice. The synchronous motions involved ultimately result in large-strain lattice deformation and a transition from an initial to a final phase on the macroscopic scale. One of the simplest bcc−fcc crystal-lographic strain paths is that of the Bain deformation.[13] It is a continuous expansion of a bcc lattice along one of the cubic axes together with a compression along the other two. When the c/a ratio (a and c are lattice parameters) reaches $\sqrt{2}$, the body-centered-tetragonal lattice becomes an fcc structure.[14]

The mesoscopic time and length scale of the martensitic transformation has limited the availability of direct, real-

time, microscopic observations. An insight into the energetics and dynamics of very fast, early processes has been obtained with the aid of molecular dynamics simulations,[15−21] but the time scale of picoseconds (ps) to nanoseconds (ns)[21] is shorter than the time required for the full transformation to take place in a real specimen. From the experimental side, conventional transmission electron microscopy (TEM) can record snapshots of the process, but with a millisecond resolution at fastest.[22] We note that the effects of laser pulse irradiation on an Fe specimen have previously been reported to induce phase changes by a sudden temperature jump[23,24] or gigantic pressure,[25,26] but observations in these studies were made only to postevent microstructures by the use of continuous-wave probes, missing detailed information on the mechanism of phase-change dynamics. On the other hand, a time-resolved study has been carried out on Fe thin films by high-speed TEM imaging with ns laser heating. This work focused on the ns and microsecond (μs) dynamics of melting, thermocapillary flow, and recrystallization of Fe in thin films.[27]

In this contribution, we report the real-time in situ visualization of iron phase transformation, from bcc to fcc, a complex solid-state transition involving collective atomic displacement and interface movement. To reveal the irreversible processes during the course of structural change, we used imaging and single-pulse diffraction in our four-dimensional (4D) ultrafast electron microscope (UEM).[28−32] This application to martensitic structural dynamics was suggested by Thomas in 2005.[33] A single optical pulse was used to induce an impulsive temperature jump in the Fe thin-film specimen, while a single pulse of many electrons was synchronized to record a frame of diffraction at a well-defined time after the initiation of the phase change. This ns single-pulse probing is different from UEM single-electron mode of operation[29−31] and has been invoked in the study of other materials;[32,34] one of them is titanium whose phase transition was studied at different temperatures.[34] The specimen with bcc structure is heated at a rate of ∼10^{11} K/s, and then cooled diffusively at a rate of ∼10^7 K/s, revealing sequential aspects of the transformation. The metastable fcc structure quenches and survives at room temperature.

Atomic movements[11] in a unit cell must be on the time scale of femtoseconds (fs), but due to the collective nature of the martensitic transformation a complex, kinetic balance between atomic lattice energetics and mesoscopic-to-macroscopic interface dynamics governs the overall process. Accordingly, a series of diffraction images, each recorded using a single ns electron packet, was suitable to capture the entire irreversible structural change spanning ns and μs. Two distinct time scales for the transformation have been unveiled, and we discuss the structures and energetics of the two corresponding processes involved in the martensitic transformation of iron.

Polycrystalline, nanofilm Fe samples were produced by RF sputtering onto 200-mesh copper TEM grids with Formvar substrates. Approximately 500 (90 μm × 90 μm) specimen areas with films of homogeneous microstructure and uniform thickness (∼58 nm) were produced in a single run. The low vacuum in the sputtering chamber (∼8×10^{-3} torr) resulted in some combination of Fe and oxygen (O). From measurements of the electron-energy-loss spectra, the relative composition of O was found to be 25% (or 8% by weight) with no other element detected. It should be mentioned that the presence of O, when less than 23% by weight, has been reported to have minimal effect on the phase-transition characteristics of iron.[35,36] Diffraction analysis allowed us to conclude that the sample is dominated by α-Fe with the diffuse residual reflections being consistent with oxides. Note that Fe_3O_4 (magnetite) is stable below ∼830 K whereas FeO (wüstite) is stable at higher temperatures.[35,36]

All experiments were performed with the second generation of UEM (UEM-2), the operation of which in the ns single-pulse mode has been described elsewhere.[32] Briefly, the output (1064 nm) of a Q-switched Nd:YAG laser was frequency-doubled to generate the 532 nm pump pulse, which was used to heat the specimen. The output of another laser at 355 nm was used to generate the electron probe pulse, which was accelerated to 200 keV. Unlike in UEM, the temporal delay in this single-pulse mode can be made arbitrarily long with electronic triggering, an essential feature of these studies. Here, the overall temporal response (∼20 ns) is used to span changes up to 150 μs (and also seconds later). All single-pulse diffraction patterns were obtained by using the selected-area diffraction aperture, which confines the measurement to an area of 25 μm in diameter on the specimen. For a typical single-pulse diffraction image reported here, about 2×10^5 electrons were detected.

For all experiments, the nominal heating-pulse energy at the specimen was estimated to be 2.8 μJ. This value and the spot size at the specimen, with a full-width at half-maximum (fwhm) of the intensity of ∼50 μm (see below), were selected to maximize the probability of producing extensive phase change across the 25 μm selected area positioned at the center of the grid square while leaving the film relatively intact. This proved to be a demanding balance to achieve. When the laser was less tightly focused, higher pulse energy was required to produce the phase change, causing the film to break more readily, presumably due to thermal stress at the edges of the specimen area. Even under the optimum chosen conditions, large variations in the extent of phase transformation and melt or ablation damage still occurred on a shot-to-shot basis, indicating high sensitivity to variability in laser power, focusing, and pointing. After setting the laser alignment to heat a desired area on the specimen, the variation in position of single-shot laser burn marks measured through the course of a day's experiments was found to have a standard deviation of ∼3 μm.

The procedure adopted for the measurement of time-resolved diffraction was to record three single-pulse images for each new specimen area, the first before the laser heating, the second (the "timed frame") at a selected ns to μs delay with respect to the heating pulse, and a third recorded seconds later. Only when the "after" diffraction pattern was assessed visually to indicate dominance of the fcc phase was the experiment considered acceptable. A postexperiment low-
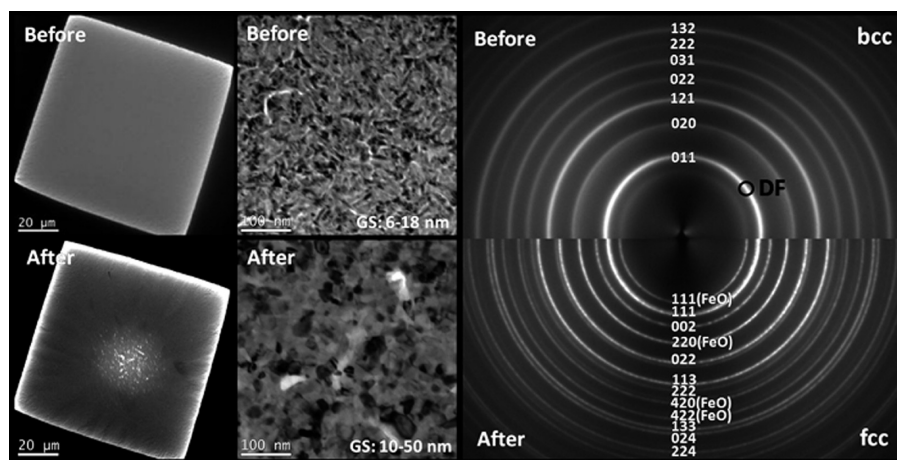
Figure 1. Morphological (image) and structural (diffraction) changes in polycrystalline Fe thin films before and after the single laser pulse treatment. In low-magnification images (left panel), a burn mark induced by single laser pulse is visible. In high-magnification images of the center of the laser focus (middle panel), the dark areas are nanocrystallites with zone axis orientation closely parallel to the incident electron beam (giving enhanced contrast). GS indicates the grain (particle) size. Note that the particle size is found to increase after the single laser pulse treatment. Electron diffraction patterns were obtained by using a selected-area diffraction aperture of 6 μm diameter positioned at the center of the laser focus. The total transformation of the diffraction pattern is clear. The rings are indexed with the bcc (before) and fcc structures (after) of Fe, respectively. Diffraction rings due to FeO are also apparent in the after diffraction (see text). The circle labeled DF indicates the position of the aperture used for the dark field image of Figure 2.

magnification image was also recorded to document the effect of the laser pulse on each of the treated film grids. In these, the position of the burn spot and the final integrity of the film could be assessed, and timed frames were excluded from the final data set if the film was found to have a hole with a diameter >7 μm.

In this way, the results entering into the analysis were obtained from those experiments for which the laser intensity distribution was relatively well-defined. For two different sets of experiments, the probe selected area was aligned to the center of the laser pulse and to a point 10 μm away from the center, respectively. Similar behavior was observed for the two sets when analyzed independently, and for the purpose of this report, data from the two sets are combined unless otherwise noted. Further detailed examination of some of the laser-heated areas by TEM imaging and diffraction was carried out to confirm the general effectiveness of the screening process, as discussed below.

Structural and morphological changes in Fe before and after a single laser pulse treatment are shown in Figure 1 for an experiment satisfying the selection criteria described above. In lower magnification images (left panel), the Fe film initially has a uniform bcc structure, and after the laser pulse heating a burn mark is apparent. High-magnification images show a change in grain size in the center of the burn. The diffraction patterns at right for a selected area of 6 μm diameter at the center of the laser focus exhibit Debye−Scherrer rings formed by numerous diffraction spots from a large number of randomly oriented, nanocrystalline particles without any texture. The difference of diffraction ring positions before and after the single laser pulse treatment is evident. Principle rings can be indexed by bcc (before) and fcc structures (after) of Fe. Several new distinct rings clearly assignable to FeO also appear in the after image.

Figure 2 depicts the dark-field (DF) image and particle (grain) size distribution of Fe nanocrystals before single-pulse laser heating. The DF image was obtained by selecting a portion of the (011) ring with an objective aperture as indicated in the diffraction pattern of Figure 1. We measured a total of 100 particles on different sample areas in both bright-field (not shown) and dark-field images. The Gaussian distribution indicated in red is centered at 11.8 ± 0.3 nm with a fwhm of 6.2 ± 0.7 nm. From these measurements, we deduce that the particle size is uniformly distributed before the single-pulse laser excitation, excluding inhomogeneous kinetics due to different-sized particles. The particle size is observed to increase after the laser pulse irradiation (see below).

Figure 3 shows an example of the variation with distance from the laser spot center of the changes induced by a single laser pulse. In the images of higher magnification in the upper panel, the grain size progression is noticeable for the positions labeled A to D in the lower magnification images. The false colors in the burn pattern in the inset reflect contrast gradient, illustrating the spatial dependence in both grain size and film morphology, apparently strongly correlated with the crystalline phase. The diameters of the red and green regions in this particular burn mark are measured to be 18 and 34 μm, respectively. The radial changes in film properties across the burn spot mirror the fluence distribution in the pulse. The electron beam size for the single-pulse electron diffraction measurements is 25 μm in diameter, which covers the region shaded in red for concentric alignment of laser and electron beam profiles.

From diffraction-pattern analysis, it is found that the crystal structure in the regions A, B, and C is 100% fcc, and in region D it is 100% bcc. The thickness of the boundary region where fcc and bcc phases coexist is measured to be approximately 1 μm, marked by the white dotted lines. The
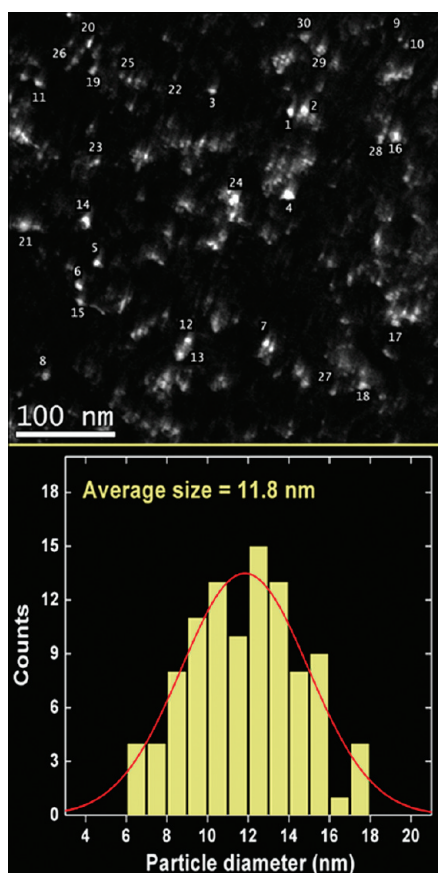
Figure 2. Dark-field (DF) image and particle (grain) size distribution of α-Fe nanocrystals without pulsed laser heating. The DF image was obtained by selecting a portion of the (011) ring with an objective aperture. One hundred particles in both bright-field and DF images are measured in total, of which 30 particles in a DF image are representatively shown. A Gaussian fit of the distribution is shown, centered at 11.8 ± 0.3 nm, with a fwhm of 6.2 ± 0.7 nm.

Figure 3. Bright-field images showing the spatial variation of morphology change of Fe nanocrystals after single-pulse laser heating. The locations for the high magnification images (top) are indicated in the burn mark pattern recorded at lower magnification in the middle panel. The false-color image shows the full response after a single laser-pulse heating. The phases in the areas A, B, C, and D were identified from the diffraction patterns, indicating the fcc and bcc structures. The red-zone (A and B) diameter is 18 μm and the green-zone diameter (C) is 34 μm. The white, dotted lines mark the boundary between the fcc and bcc phases. A radial distance axis for the middle panel with a calculated initial temperature distribution (see text) is presented at the bottom. In the high magnification images (upper panel), the grain size distribution follows the laser-heating distribution.

fcc limit coincides here with the total apparent burn mark (green zone) with the transition being 17 μm from the burn center. It should be noted that burn mark patterns can be elongated and the mean diameters obtained from visual inspection of a small random selection of single-pulse experiments varied from 34 to 45 μm with a typical radius of 19 μm. A representative temperature profile of a specimen immediately after laser heating, as deduced from our data (see below), is also shown in Figure 3 with the radial zones corresponding to the temperature ranges of different crystal phases indicated.

A selection of the single-pulse diffraction frames taken during the phase transition is shown in the top panel of Figure 4. Each diffraction frame was obtained from a fresh region of the specimen, by translation in the specimen plane. The depletion of well-defined diffraction rings of bcc, α-Fe, a transition to broad and indistinct scatter intensity, and the eventual growth of new sharp rings of fcc, γ-Fe are evident in the series of images recorded at different time delays. Accordingly, a series of these frames becomes a movie for the bcc to fcc phase transformation. At a glance, it is observed that at $t = 25$ ns, the intensities of the (020) and (121) rings of bcc are reduced and its (011) ring is somewhat
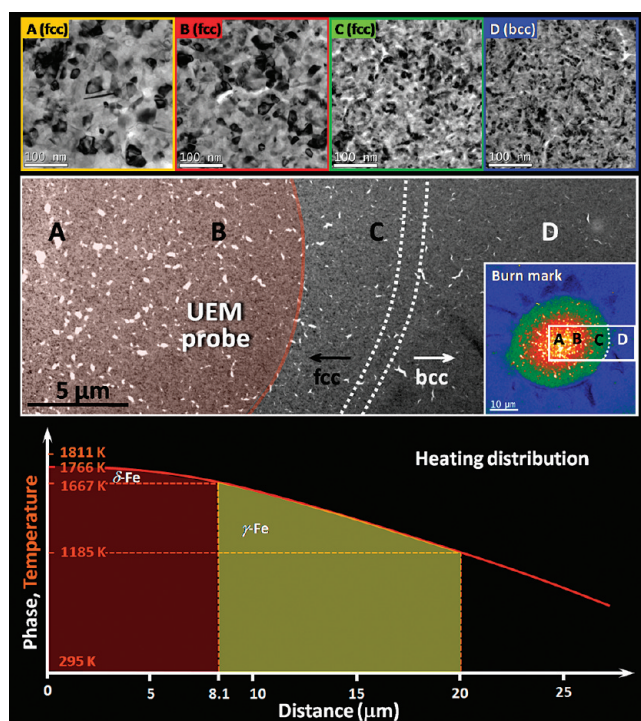
broadened. With time, new fcc diffraction rings appear, directly observable in the frames (without need for data processing). The indexing of the first and last images can be compared to that of the TEM diffraction in Figure 1 in which the higher electron counts give more intense and more sharply focused rings.

To quantify the spatiotemporal behavior, radial diffraction profiles were constructed from the rotational averages of the diffraction images, each normalized to its total electron count. Through the acquisition of a series of diffraction snapshots, the in situ martensitic transformation of Fe is now visualized. The overall time evolution of the radial diffraction profiles is displayed in the bottom panel of Figure 4. Clearly evident in the 3D surface plot are the in situ structural changes revealed by the time-dependent shift of diffraction peaks in the dynamic range of ns and μs. Representative radial diffraction profiles at selected times are presented in the left panel of Figure 5. At negative time, that is, before the arrival of a heating pulse, the characteristic diffraction rings of the room temperature bcc, α-Fe are shown. A snapshot of the transformation evolution at 25 ns after the heating laser pulse indicates that the bcc, α-Fe phase is promoted to a hot bcc structure, as deduced from the decrease of reciprocal lattice
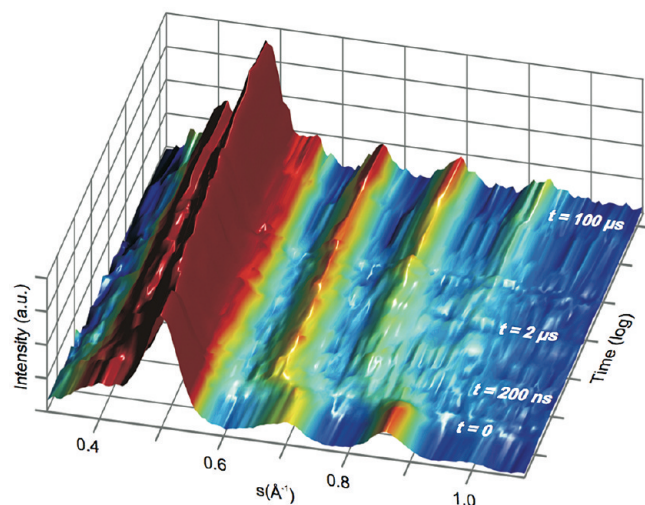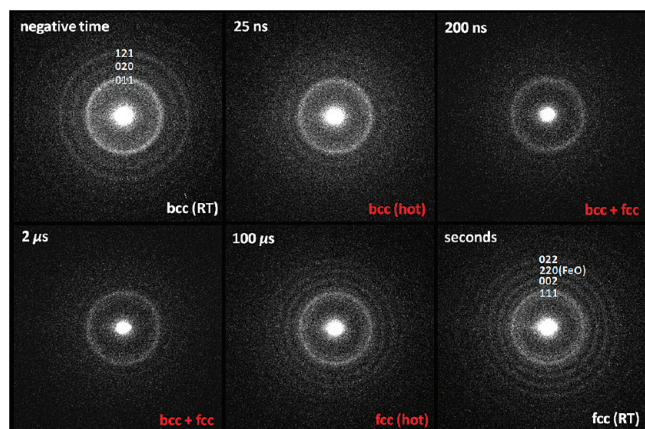
Figure 4. (Top) Snapshots of transient diffraction reflecting the complex structural changes that Fe undergoes after optical excitation and heating. Shown are six representative single-pulse diffraction images at different time delays. Each still frame has an exposure time of 15 ns. For details, see text. (Bottom) Map of time-dependent diffraction evolution. Shown are the rotationally averaged diffraction patterns taken at 33 different times from two independent sets of data and plotted as a 3D surface. This surface shows clearly the changes that happen to the different diffraction peaks as a function of time. At negative time the bcc, α-Fe is dominant and at hundreds of μs the pattern approaches the asymptotic fcc, γ-Fe.

spacings and the increase of diffraction ring widths; the consequences of heating in crystallography are the expansion of lattice and the increase of atomic vibration. The $2.6 \pm 0.4\%$ increase of lattice spacings at $t = 25$ ns is equal to the expansion measured for an Fe specimen at thermal equilibrium just below its melting point,[37,38] consistent with the choice of pulse energy near the upper threshold for the survival of intact films.

In a frame at $t = 100$ μs, new broad rings clearly appear. The image reflects the complete structural change from bcc to hot fcc (γ-Fe). The temperature of the fcc phase at $t = 100$ μs is deduced to be 1000 ± 300 K from comparison of the lattice spacing with extrapolation of steady-state literature values.[37] Finally, the diffraction patterns at seconds after heating (asymptote) display the complete quenching (by rapid cooling to room temperature) of the metastable fcc phase as reflected in the decrease of lattice spacings and sharpening of diffraction rings, compared to those observed at $t = 100$

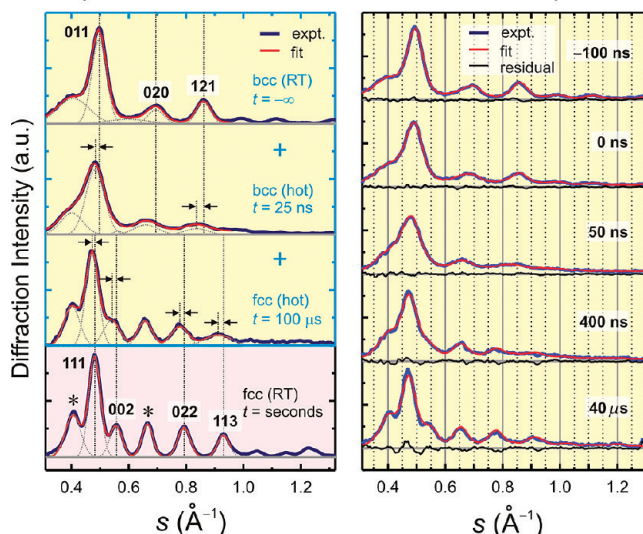## Experimental Diffraction and Phase Composition

Figure 5. Time frames of diffraction. (Left) Radial diffraction profiles of four discrete structures in the phase transformation. The result of a fit of each diffraction profile to a sum of Gaussian peaks is shown, together with plots of the constituent peaks. Asterisks denote diffraction rings from FeO. (Right) Real-time capture of single-pulse diffraction during the phase transformation. Also depicted are the linear combinations of three reference diffraction spectra of bcc (α-Fe), hot bcc, and hot fcc (γ-Fe) to fit the time-framed diffraction. As an indication of the quality of the fits, the differences between transient diffraction profiles and the fits are shown as well.

μs. Rings not assignable to γ-Fe, such as the two marked by asterisks in the figure are attributed to FeO, formed at a high temperature and quenched by the rapid cooling. In the radial diffraction profile at $t = 25$ ns, distinctive features of fcc structure, for example, the two diffraction rings from the (002) and (022) planes, are absent. Similarly, the diffraction at $t = 100$ μs lacks a strong diffraction ring from the (121) plane of bcc. Therefore, the two radial diffraction profiles taken at $t = 25$ ns and 100 μs are designated as representative of the hot bcc and fcc phases, respectively. This identification, that is, 100% bcc at 25 ns and 100% fcc at 100 μs, indicates that the phase transition occurs completely within the dynamic range of this study. Only the cooling of the quenched fcc phase occurs at longer times.

The course of the phase transformation can be tracked from a fit of time-framed radial diffraction profiles to linear combinations, following Vegard's law,[32,39] of three of the reference diffraction spectra discussed above: (1) negative time (α-Fe); (2) 25 ns (hot bcc); and (3) 100 μs (hot fcc, γ-Fe). A selection of radial profiles for different time delays is shown in the right panel of Figure 5, along with the fits and residuals from the fitting process. The fits are satisfactory at all time delays measured, suggesting the interconversion between the two discrete phases after heating. By obtaining fractions of each phase for a series of time delays, we reconstructed the time-dependent content changes of the different phases. In Figure 6, the extracted fractions from the combination of two sets of experiments are plotted as a function of delay time. These show a response-limited rise of hot bcc, followed by a decay of bcc content in favor of
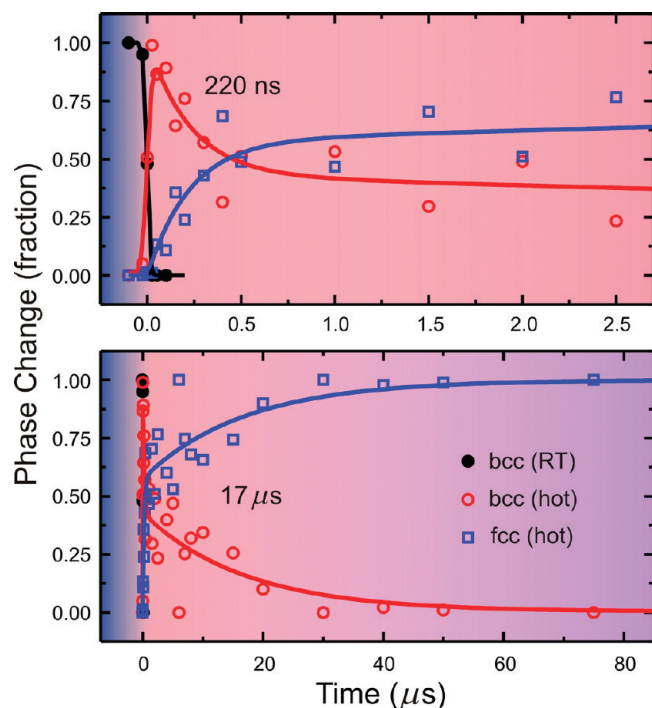
Figure 6. Evolution of in situ martensitic transformation in Fe. Phase-content kinetic profiles of the transformation at short (top) and long (bottom) time scales. The depletion of the initial bcc, α-Fe by the ns heating pulse is within our instrumental response function of ~20 ns. Biexponential functions are used to simulate the time-dependent changes between bcc and fcc phases. Heat diffusion dynamics in the specimen is pictorially presented as a color change in the background of the plots. Note that the time scale of the fast process (220 ns) is much shorter than the μs time scale of heat transport for the Fe specimen (see text).

fcc, with full conversion completed by around 30 μs. A fit of the time evolution of the fall in bcc and rise in fcc reveals two characteristic time constants of 220 ± 70 ns ($58 \pm 6\%$) and 17 ± 6 μs ($42 \pm 6\%$). It is worth mentioning that the observation of two distinct time regimes is robust when applying a variety of different standards in the selection of experiments to include in the analysis. The fractions and rates can vary substantially, however, because the determination of the relative content of bcc and fcc structure is subject to the large uncertainty evident in the scatter of the data plotted in Figure 6.

The effect of probe alignment was also examined by analyzing separately the two sets of data acquired with a mean difference in selected area location of 10 μm. Each shows a biphasic time evolution similar in appearance to that in Figure 6 but with some difference in time constants and component fractions. For central probing, the fit parameters obtained are 210 ± 80 ns ($52 \pm 7\%$) and 15 ± 5 μs ($48 \pm 7\%$), while probing on average 10 μm from the laser center produced a fast component that appeared slower and more dominant with lifetime and conversion fraction of 330 ± 80 ns and $70 \pm 7\%$. With its small amplitude of ≤30%, the long component for the off-center probe was not well determined but could be fit to a lifetime of 15 to 25 μs.

Before discussing the mechanism, the effect of the heating pulse on the Fe film should be considered. When the

specimen absorbs an optical pulse, the lattice energy, converted from ballistic heating of the valence electrons and energy transfer to phonons in a few ps, builds up in the illuminated area.[30,40] Consequently, the irradiated region will heat up rapidly following phonon−phonon interaction on the time scale of tens of ps, implying that the temperature of the specimen will immediately change during the ns illumination; this description conforms to our finding of very hot bcc structure at 25 ns delay. Our observations of film damage and morphology change clearly indicate a laser-induced temperature distribution near the melting point at the center and above the temperature of 1185 K required for fcc formation out to a radius of ~19 μm.

An estimate of the temperature distribution after the laser pulse can be made from knowledge of the characteristics of the laser pulse and the thermal and optical properties of Fe: the real and imaginary parts of the refractive index of Fe (at 2.4 eV, $n = 2.56$ and $k = 3.31$, respectively)[41] giving absorbance of 0.42 for a 58 nm thick film;[42] average heat capacity of 0.68 J/(g·K);[38] room-temperature density of 7.88 g/cm^3; latent heats of transformation;[38] and a pump pulse energy at the specimen of 2.8 μJ. We find that for a 47 μm excitation spot size whose temperature distribution is displayed in Figure 3, all observed behavior can be explained in a self-consistent manner. Specifically, under this illumination (peak fluence of 113 mJ/cm^2) the maximum temperature reached is 1766 K, slightly below the melting temperature, and the region in which sufficient energy is available immediately after the pulse to initiate the phase change to fcc extends to a radius of 20 μm. The initial temperatures will be the maximum temperatures reached in all regions of interest, since thermal diffusion causes only cooling out to a radius of 28 μm at which point the fluence is down to 37% of the peak value and no phase or morphology change occurs.

For the above-described temperature profile, the area out to a radius of 8.1 μm, representing 42% of the area of a concentrically aligned probe region, is heated sufficiently to reach a temperature above the range of the fcc, γ-Fe phase (1185 to 1667 K) at equilibrium. The initial temperature of the remaining 58% of the probe area lies within the fcc range (see Figure 3). Thus the following two characteristic populations are observed: one, in an annulus from 8.1 to 12.5 μm, is at a temperature for which the transformation from the bcc to the fcc structure is immediately thermodynamically favored, while another population must cool through the heat-diffusion process before it can undergo that transformation. The mean initial temperatures of the two populations are 1592 and 1716 K, and their fractions for concentric probe alignment, assuming proportionality to area, are 58 and 42%, respectively. The faster component of the fcc appearance (220 ns), accordingly, represents the first population, giving the rate of the direct solid−solid phase transformation process, that is, martensitic transformation, whereas in the same model the 17 μs rise is the rate-limiting cooling step for the indirect transformation of the second, hotter population.[43] It is mainly during the annealing of bcc in this cooling period of μs duration at temperatures above 1667 K that grain

size is expected to increase, as seen in regions A and B of Figure 3. In region C, which has never been heated above 1667 K, the average fcc grain size is similar to that of the parent bcc phase.

Support for this conclusion regarding the origin of the two rate constants is provided by a comparison of the respective fractions derived from the two sets of data with different probe location. A displacement away from a concentric alignment of the probe position by more than 4 μm is expected to cause a drop in the contribution of the long-lived component. For a 10 μm displacement, the overlap of the hot center of the laser spot with the probe area is calculated to fall from 42 to 26%, qualitatively in line with the observation. It should be noted, however, that the calculations also show a very high sensitivity of the population fractions to laser spot size, which is undoubtedly a contributing factor in the level of noise in the experimental data.

The central questions pertinent to the mechanism are the following: what determines the time scale, and what is the nature of the elementary processes of the diffusionless transformation? The overall rate of a martensitic transformation reflects the probability of nucleus formation and the specific rate of particle growth. The probability of collective displacements among many unit cells is the key for creating a deformation path from bcc to fcc. Upon heating, the generation of coherent phonons could be a motif of the martensitic transformation.[44] In this scheme, for 10 nm nanocrystallites (Figure 2) the overall transformation is expected to be on the time scale of $10-100$ ps with a typical interface mobility of $100-1000$ m/s.[11,19−21] However, these time scales are 3 orders of magnitude shorter than the observed ns scale. In addition, coherent phonons are generally produced by intense fs laser excitation having duration shorter than the half period of lattice vibrations, and they typically damp out in ten(s) of ps.[45] With the use of impulsive ns heating in this study, the phonons of the lattice must be regarded as incoherent, and the ordered motions involving collective displacement must emerge from such incoherent state of the system through stochastic fluctuations.

After the initial heating, each expanded lattice of a bcc structure can follow different Bain deformation directions to form the fcc structure (Figure 7).[14,20] The transformation is a time-dependent process, initially barrier-controlled when the embryonic nucleation is being established, and barrierless at longer times when the grain growth is controlled simply by the speed of sound. The process can be described by multiple "sub-activation" barriers[21] with a global-minimum search on the energy landscape. Once the nucleus has reached a critical size that is big enough to lower the energies of the sub-barriers for additional nucleation, then the propagation of the new fcc phase can rapidly follow at the velocity of sound to complete the martensitic transformation (see the inset of Figure 7). The transformation rate can thus be expressed as

$$k = k_0 \exp(-\Delta G^{\ddagger}/k_{\mathrm{B}}\mathrm{T})$$

where k is the rate of martensitic transformation and k_0 is

given by a typical lattice vibration frequency; k_{B} is the Boltzmann constant. In this picture, $\Delta G^{\ddagger}$ is the free energy of nucleation.

The global activation energy for the phase transition is determined by the probability of nucleation for which a series of jumps by a group of atomic displacements among multiple unit cells are prerequisite. Using the observed time constant of 220 ns and the average temperature in the area undergoing direct transformation ($\sim$1590 K), we obtained the free energy of nucleation to be in the range of $1.7-2.0$ eV, when k_0 is in the range of $10^{12}-10^{13}$ s^{-1}.[11,17−21] This obtained value is similar to those reported theoretically and experimentally from post-transform observations at different temperatures.[9,10] Note that the sum of nonchemical free energy including interfacial energy, strain energy, and elastic deformation energy in the martensitic transformation of Fe is known to be of the order of $\leq$10 meV.[11] Lastly, when the barrier is lowered by nucleation and k approaches k_0, the typical speed of sound suggests grain growth to be on the ps time scale for nanometer scale grains.
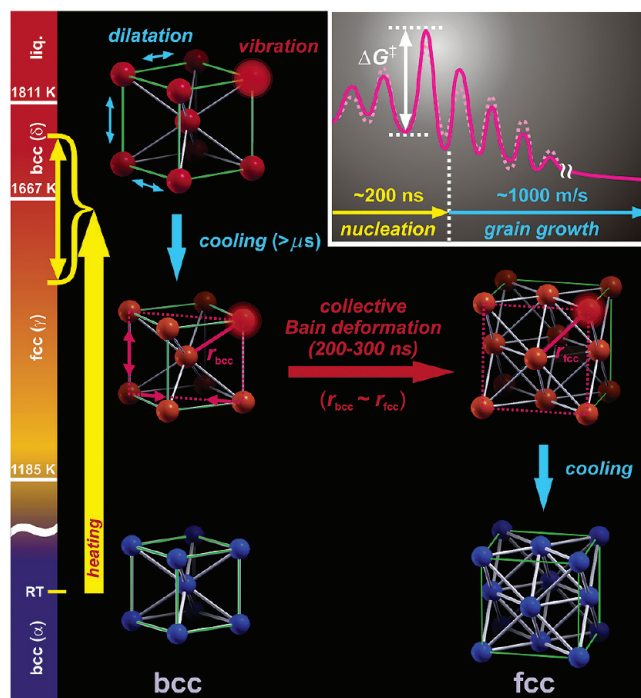

Figure 7. Summary of the martensitic transformation of Fe induced by a ns heat pulse. Upon absorption of the laser pulse, α-Fe is instantly heated above 1185 K. Below 1667 K, it undergoes the solid-state phase transformation from bcc to fcc on the time scale of 200 to 300 ns. For heating above 1667 K into the temperature range in which bcc, δ-Fe is thermodynamically more stable, a cooling process in μs must proceed prior to the fast structural change. After hundreds of μs, the fcc phase is quenched at room temperature. (Inset) Schematic energetics of martensitic transformation on the basis of a transition-state theory. The overall activation energy, $\Delta G^{\ddagger}$, is the difference between the maximum energy of the system and the energy of the initial state. Nucleation and grain growth (interface movement) are shown on a single reaction coordinate and the activation barriers for sub intermediate states can be variable due to the effect of the fluctuating local matrix around displacing atoms in a lattice. With nucleation, the subactivation barriers are expected to decrease due to the inductive nature of crystallinity.

In most Fe-based materials, the time scale of a martensitic transformation has been reported to be on the order of ∼100 ns, as obtained from bulk measurements of electric resistance and magnetization.[11] According to our picture, the rate of a martensitic transformation can change with the number of nuclei formed; assuming that one nucleus forms in each grain, for grains smaller than 10 μm the rate-determining step is the nucleation, and the rate is expected to depend on temperature. In this study, the change in rate found by separating the data into concentric and peripheral probe sets offers a limited test of the expected temperature-dependency. When probing off-center, the mean temperature of the monitored population does certainly go down, and the extracted rate of the solid-state transformation decreases, which is a change in the expected direction. Although the noise in the experiment leaves the result uncertain, modifications in the experiment design (see below) could address this issue in a definitive manner. Only for grains bigger than tens of μm (≥ 100 m/s × 100 ns), can the grain growth determine the overall transformation showing a weaker temperature dependence.

It is noteworthy that a relatively long incubation time was reported in a recent molecular dynamics simulation to be essential to the formation of interfaces, which then start to move very rapidly to complete the martensitic transformation; the formation of the interface structure, that is, "nucleation" in this study, required for the transformation strongly depends on the driving force.[21] A more open interface structure, for example, vacancies and dislocations, is expected to increase the probability of collective atomic motions and, thus, to lead to more facile transformation. This notion is in accordance with conclusions drawn for decades from postevent studies of imaging and crystallography of Fe microstructures.[11]

In conclusion, the martensitic phase transformation from bcc to fcc in polycrystalline Fe has been initiated by impulsive heating and its evolution observed in real time by single-pulse 4D electron microscopy. The results reveal a 200−300 ns direct transformation channel, as well as a cooling-limited channel, which occurs on the μs time scale. The potential to examine this and analogous processes by the UEM methodology is apparent. Variation in the specimen dimensions, laser focus, pulse energy, and probe position can provide the opportunity to define the distribution and evolution of specimen temperature. Moreover, investigation of rate dependence on initial film morphology and grain size, as predicted in the model presented here, should also be possible. Given the great importance of Fe and the unique nature of martensitic transformations, this report is only the first for such investigations.

References

(1) Bolm, C. *Nat. Chem.* **2009**, *1*, 420.
(2) Saxena, S. K.; Dubrovinsky, L. S. *Am. Mineral.* **2000**, *85*, 372–375.
(3) Andrault, D.; Fiquet, G.; Kunz, M.; Visocekas, F.; Häusermann, D. *Science* **1997**, *278*, 831–834.
(4) Belonoshko, A. B.; Ahuja, R.; Johansson, B. *Nature* **2003**, *424*, 1032–1034.
(5) Laio, A.; Bernard, S.; Chiarotti, G. L.; Scandolo, S.; Tosatti, E. *Science* **2000**, *287*, 1027–1030.
(6) Porter, D. A.; Easterling K. E. *Phase Transformations in Metals and Alloys*; Chapman & Hall: London, 1992.
(7) Headley, T. J.; Brooks, J. A. *Metall. Mater. Trans. A* **2002**, *33A*, 5–15.
(8) Massalski, T. B.; et al. *Binary Alloys Phase Diagrams*; ASM International: Materials Park, OH, 1990.
(9) *Martensite: a Tribute to Morris Cohen*; Olson, G. B., Owen, W. S., Eds.; ASM International: Materials Park, OH, 1992, and references therein.
(10) Christian, J. W. *The Theory of Transformations in Metals and Alloys*; Pergamon Press: London, 2002.
(11) Nishiyama, Z. *Martensitic Transformation*; Academic Press: New York, 1978.
(12) Bhattacharya, K.; Conti, S.; Zanzotto, G.; Zimmer, J. *Nature* **2004**, *428*, 55–59.
(13) Bain, E. C. *Trans. Am. Inst. Min., Metall. Pet. Eng.* **1924**, *70*, 25–35.
(14) Krasko, G. L.; Olson, G. B. *Phys. Rev. B* **1989**, *40*, 11536–11545.
(15) Kadau, K.; Germann, T. C.; Lomdahl, P. S.; Holian, B. L. *Science* **2002**, *296*, 1681–1684.
(16) Entel, P.; Meyer, R.; Kadau, K. *Philos. Mag. B* **2000**, *80*, 183–194.
(17) Osetsky, Y. N.; Serra, A. *Phys. Rev. B* **1998**, *57*, 755–763.
(18) Sinclair, C. W.; Hoagland, R. G. *Acta Mater.* **2008**, *56*, 4160–4171.
(19) Tateyama, S.; Shibuta, Y.; Suzuki, T. *Scr. Mater.* **2008**, *59*, 971–974.
(20) Bos, C.; Sommer, F.; Mittemeijer, E. J. *Modell. Simul. Mater. Sci. Eng.* **2006**, *14*, 273–282.
(21) Bos, C.; Sietsma, J.; Thijsse, B. J. *Phys. Rev. B* **2006**, *73*, 104117.
(22) Boyes, E. D.; Gai, P. L. *Ultramicroscopy* **1997**, *67*, 219–232.
(23) Teodorescu, V. S.; Nistor, L. C.; Van Landuyt, J.; Dinescu, M. *Mater. Res. Bull.* **1994**, *29*, 63–71.
(24) Teodorescu, V. S.; Mihailescu, I. N.; Dinescu, M.; Chitica, N.; Nistor, L. C.; Van Landuyt, J.; Barborica, A. *J. Phys. IV* **1994**, *4*, C4−127−130.
(25) Yaakobi, B.; Boehly, T. R.; Meyerhofer, D. D.; Collins, T. J. B.; Remington, B. A.; Allen, P. G.; Pollaine, S. M.; Lorenzana, H. E.; Eggert, J. H. *Phys. Rev. Lett.* **2005**, *95*, 075501.
(26) Kalantar, D. H.; Belak, J. F.; Collins, G. W.; Colvin, J. D.; Davies, H. M.; Eggert, J. H.; Germann, T. C.; Hawreliak, J; Holian, B. L.; Kadau, K.; Lomdahl, P. S.; Lornzana, H. E.; Meyers, M. A.; Rosolankova, K.; Schneider, M. S.; Sheppard, J.; Stölken, J. S.; Wark, J. S. *Phys. Rev. Lett.* **2005**, *95*, 075502.
(27) Balandin, V. Y.; Otte, D.; Bostanjoglo, O. *J. Appl. Phys.* **1995**, *78*, 2037–2044.
(28) Zewail, A. H.; Lobastov, V. Method and System for Ultrafast Photoelectron Microscope. U.S. Patent 7,154,091 B2, 20050401, 2006.
(29) Shorokhov, D.; Zewail, A. H. *Phys. Chem. Chem. Phys.* **2008**, *10*, 2879–2893.
(30) Barwick, B.; Park, H. S.; Kwon, O.-H.; Baskin, J. S.; Zewail, A. H. *Science* **2008**, *322*, 1227, and references therein.
(31) Park, H. S.; Baskin, J. S.; Barwick, B.; Kwon, O.-H.; Zewail, A. H. *Ultramicroscopy*, in press (doi: 10.1016/j.ultramic.2009.08.005).
(32) Kwon, O.-H.; Barwick, B.; Park, H. S.; Baskin, J. S.; Zewail, A. H *Proc. Natl. Acad. Sci. U.S.A.* **2008**, *105*, 8519–8524.
(33) Thomas, J. M. *Angew. Chem., Int. Ed.* **2005**, *44*, 5563–5566.
(34) LaGrange, T.; Campbell, G. H.; Turchi, P. E. A.; King, W. E. *Acta. Mater.* **2007**, *55*, 5211–5224.
(35) Darken, L. S.; Gurry, R. W. *J. Am. Chem. Soc.* **1945**, *67*, 1398–1412.
(36) Darken, L. S.; Gurry, R. W. *J. Am. Chem. Soc.* **1946**, *68*, 798–816.
(37) Kohlhaas, R.; Dünner, Ph.; Schmitz-Pranghe, N. *Z. Angew. Phys.* **1967**, *23*, 245–249.
(38) *Metals Handbook*, 10th ed.; ASM International: Materials Park, OH, 1990; Vol. 2, pp 1118−1131.
(39) Denton, A. R.; Ashcroft, N. W. *Phys. Rev. A* **1991**, *43*, 3161–3164.
(40) Hartland, G. V. *Annu. Rev. Phys. Chem.* **2006**, *57*, 403–430.
(41) Lide, D. R. *Handbook of Chemistry and Physics*; CRC Press: Boca Raton, FL, 2001.
(42) *American Institute of Physics Handbook*, 3rd ed.; Gray, D. E., Ed.; McGraw-Hill: New York, 1972.
(43) In a very simple description, the time for completion of the cooling-limited transformation process should be the approximate time required for the maximum temperature on the axis of the heated distribution (∼1766 K) to fall below 1667 K, at which temperature the direct transformation proceeds on a sub-μs time scale. Experimentally,

transient diffraction measured 100 μs after impulsive heating shows that the mean temperature of the entire monitored region is still ~700 K above room temperature, roughly 600 K below the initial mean excess temperature, so the duration of about 30 μs apparent in Figure 6 for the slow phase is somewhat longer than would be predicted for the required drop of 100 K. For a theoretical comparison, we have calculated the initial rate of cooling on the axis of a Gaussian temperature distribution by thermal diffusion in an infinite 2D iron film at 1766 K. Using $\lambda = 34.2$ W/(m·K),[41] we find the time $t_{1/2}$ for the temperature to fall to half its initial value is 32 μs. On the basis of the initial slope of cooling, this calculation predicts 10% cooling in 3.2 μs, much shorter than the observed time for the slow process

to be completed. However, imperfections in the thermal continuity of the film, which are evident in high-magnification images (see Figures 1 and 3), are expected to retard the diffusion process relative to the ideal theoretical calculation, consistent with the observation. Moreover, it is evident from this calculation that the process associated with the 220 ns time constant is complete before significant diffusive cooling of the heated specimen can occur.

(44) Zhang, J.-m *J. Phys. F: Met. Phys.* **1984**, *14*, 769–783.

(45) Hase, M.; Kitajima, M.; Constantinescu, A. M.; Petek, H. *Nature* **2003**, *426*, 51–54.